Steady-State Analysis of the DR-MMC Based Hybrid Topology for Offshore Wind Power Transmission

Lu Chen, *Student Member, IEEE*, Jinyu Wang, *Member, IEEE*, Zhixiang Li, *Graduate Student Member, IEEE*, Chenyu Guo, *Student Member, IEEE*, Bobo Zhang, *Student Member, IEEE*, and Zhijie Li, *Student Member, IEEE*

***Abstract*—The hybrid topology with a modular multilevel converter and diode rectifiers connected in series (DR-MMC) has emerged as a promising solution for offshore wind power transmission. Accurate steady-state analysis is critical for the parameter design, device selection, and performance evaluation of the DR-MMC. However, existing steady-state analysis methods for this topology demonstrate considerable errors due to insufficient consideration of the DR commutation process and the neglect of the intercoupling between the DR and MMC. This article presents a more elaborate description of the DR commutation process within the DR-MMC by taking into account the dc current ripple, ac-side equivalent series resistance, and the coupling from the MMC. Building upon this, a novel steady-state model constituted by double loops is developed for the DR-MMC. Specifically, the commutation process of the DR and the power conservation of this hybrid topology together form the outer loop, whereas the steady-state model of the individual MMC serves as the inner loop. Experimental results from a scaled-down prototype validate that the proposed steady-state model can determine the electrical quantities of the DR-MMC accurately across its entire operating range.**

***Index Terms*—Commutation process, diode rectifier (DR), modular multilevel converter (MMC), offshore wind power transmission, steady-state analysis.**

I. Introduction

DUE to the superiority of wind energy resources, offshore wind farms are rapidly constructed toward the far-reaching sea. The high voltage dc (HVdc) transmission system has been recognized as a preferred solution for offshore wind power transmitting due to its less power loss and reactive power in comparison with the ac transmission system [1].

The HVdc transmission system based on the modular multilevel converter (MMC) has come to broad academic notice due to its excellent modularity, high controllability, and superior harmonic performance [2]. However, such a system exhibits large volume, heavy weight, and high cost. To make up for these drawbacks, the HVdc system based on the diode rectifier (DR) was proposed in [3]. Nevertheless, owing to the inherent uncontrollability of the DR, the black start [4], as well as harmonic currents and reactive power issues [5], cannot be solved without additional equipment in such an HVdc system. To combine the strengths of the DR and the MMC, a hybrid topology based on a parallel connection of them was presented in [6]. However, the high voltage requirement of the MMC in this topology poses challenges in realizing a small-capacity design and reducing the overall cost. Consequently, authors in [7], [8], and [9] proposed another hybrid topology, which is based on a series connection of the DR and the MMC (DR-MMC), as shown in Fig. 1(a). In practical operation, the point of common coupling (PCC) voltage is established by the MMC through closed-loop control, whereas the total dc-link voltage U_{dc0} is controlled by the inverter station. Since the MMC only needs to transmit part of the wind farm power and undertake a portion of the total dc-link voltage, the topology shown in Fig. 1(a) can reduce the power and voltage levels of the MMC to a large extent on the premise that the PCC voltage is controllable. This hybrid topology is also the focus of this article.

To design circuit parameters, select power devices, and evaluate operation performance for the DR-MMC, it is essential to obtain its electrical quantities in the steady state. For the steady-state models of the individual MMC, a great deal of work has been done in existing literature. Wang et al. [10] and Liu et al. [11] calculated electrical quantities by multiplying the switching function in the time domain. The dynamic phasor (DP) model, incorporating zero sequences, fundamental frequency DQ, and double fundamental frequency DQ2 frames, was explored in [12] and [13]. Utilizing the harmonic state-space modeling method, the harmonics present in the expression of electrical quantities can be extended to any required frequency [14], [15]. As for the steady-state models of the individual DR, Das et al. [16] represented the ac-side current by combining two sine waves with a trapezoidal wave. Additionally, the ac-side current waveform was further detailed in the time domain in [17], followed by the calculation of various frequency components through fast Fourier transform (FFT). The authors in [18] and [19] established a state-space averaging model that accounts for the time-variant switching behavior of the DR. Furthermore, Liu et al. [20] and Deriszadeh et al. [21] proposed a DP model for the DR with the linearized switching function. Moreover, Zhang et al. [22] utilized the actual sinusoidal one to avoid the error caused by linearization approximation. Nevertheless,

Received 17 May 2024; revised 29 August 2024; accepted 15 October 2024. Date of publication 18 October 2024; date of current version 18 December 2024. This work was supported by the National Key Research and Development Plan Project 2021YFB1507004. Recommended for publication by Associate Editor E. Babaei. *(Corresponding author: Jinyu Wang.)*

The authors are with the State Key Laboratory of Electrical Insulation and Power Equipment, Xi'an Jiaotong University, Xi'an 710049, China (e-mail: chenlu980425@stu.xjtu.edu.cn; wangjinyu@xjtu.edu.cn; lizhixiang951206@stu.xjtu.edu.cn; gcy20000808@stu.xjtu.edu.cn; zbb1027@stu.xjtu.edu.cn; l08281203@stu.xjtu.edu.cn).

Color versions of one or more figures in this article are available at https://doi.org/10.1109/TPEL.2024.3483928.

Digital Object Identifier 10.1109/TPEL.2024.3483928

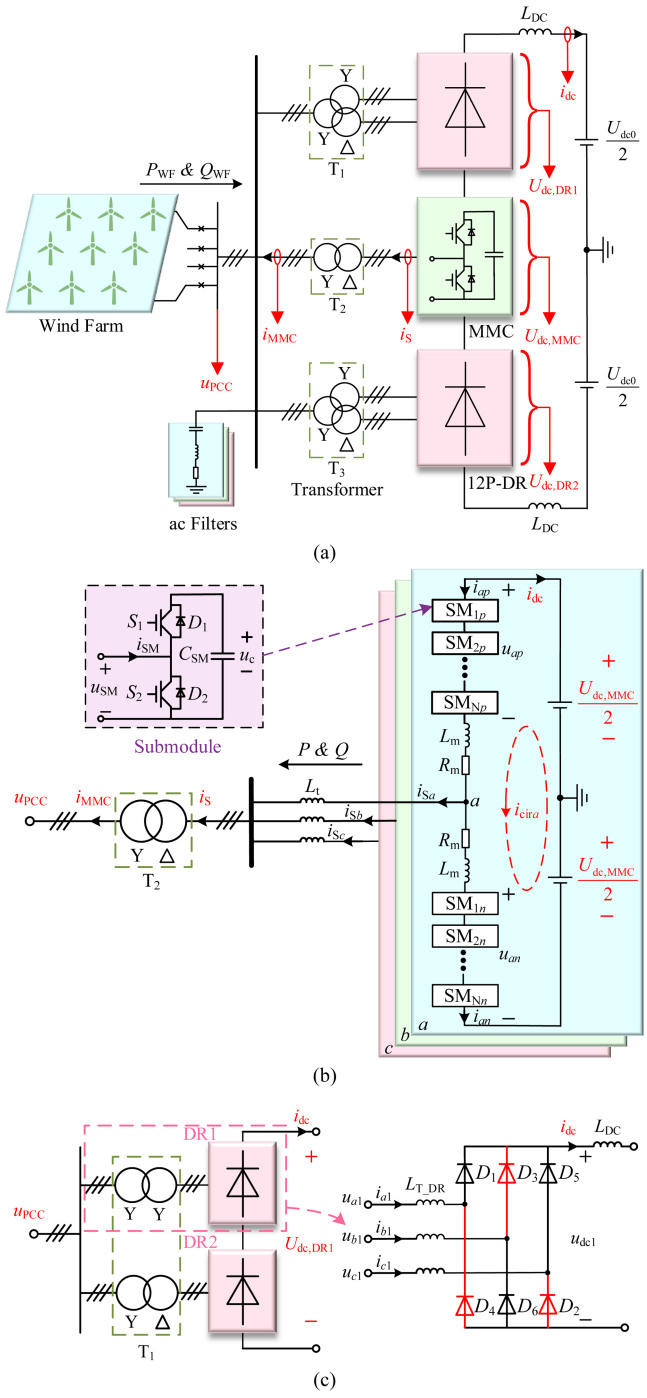

Fig. 1. Configuration of the DR-MMC. (a) Overall structure. (b) Circuit configuration of the MMC. (c) Topology of the 12-pulse DR.

the research with regard to the steady-state models for the whole DR-MMC is still in the preliminary stage. Li and Xu [23] introduced an equivalent circuit of the DR-MMC, which is a simple addition of the DR and MMC. More specifically, the DR and MMC in this hybrid topology are considered to be decoupled from each other. The electrical quantities of the DR and MMC, therefore, are calculated separately by their respective steady-state models.

Nevertheless, in conventional steady-state models, the overlap angle of the DR is calculated using only the dc component of the dc-side current [24], disregarding the effect of the dc current ripple and ac-side equivalent series resistance (ESR) on the commutation process. This omission results in considerable errors in calculating electrical quantities of the DR within the DR-MMC. Additionally, the MMC's arm inductance can alter the dc current ripple and further affect the calculation of the DR's electrical quantities. Moreover, the dc current ripple generated by twelve-pulse DRs will introduce same-frequency components into the MMC's circulating current, further affecting its electrical quantities. Such intercoupling between the DR and MMC is also neglected by conventional DR-MMC models. Therefore, a more elaborate DR commutation process as well as the intercoupling between the DR and MMC should be considered for a more accurate steady-state analysis of the DR-MMC. If so, however, the conventional models, which consider only the dc component of the dc-side current in the calculation of the overlap angle and treat the DR and MMC as independent converters, become inapplicable.

In this article, a novel steady-state model based on an elaborate description of the DR commutation process and constituted by double loops is proposed for the DR-MMC. The novelty and main contributions of this article can be summarized as follows.

1) An elaborate description of the DR commutation process within the DR-MMC is established by taking into account the effect of the dc current ripple, ac-side ESR, and the coupling from the MMC, facilitating a more accurate steady-state analysis of the entire DR-MMC.
2) A more accurate steady-state model constituted by double loops is developed for the DR-MMC. Specifically, the commutation process of the DR and the power conservation of this hybrid topology together form the outer loop, whereas the steady-state model of the individual MMC serves as the inner loop.

The rest of this article is organized as follows. Section II briefly reviews the circuit configuration and conventional analysis methods of the DR-MMC. Then, in Section III, the elaborate description of the DR commutation process is established, whereafter the complete steady-state model of the DR-MMC constituted by double loops is developed. Section IV presents the experimental results to verify the effectiveness and accuracy of the proposed steady-state model. Finally, Section V concludes this article.

II. Review of the Circuit Configuration and Conventional Steady-State Analysis of the DR-MMC

A. Circuit Configuration of the DR-MMC

The overall structure of the DR-MMC has been shown in Fig. 1(a). It consists of two identical 12-pulse DRs (12P-DRs) and one MMC. The ac-sides of the MMC and DRs are connected in parallel via link transformers (T_1, T_2, T_3), whereas their dc-sides are connected in series. In addition, a set of passive power filters is configured on the PCC to compensate for the harmonics (mainly in the 11th and 13th orders [5]) as well as the reactive power generated by 12P-DRs.

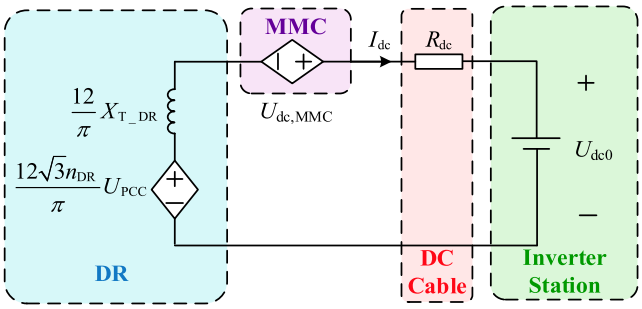

Fig. 2. Conventional equivalent circuit of the DR-MMC.

Fig. 1(b) presents the circuit configuration of the MMC, where each arm is made up of N half-bridge SMs and one arm inductor in series. Therein, i_{MMC} and i_s represent the currents of the primary and secondary sides of the link transformer, respectively, and L_{m} and R_{m} denote the arm inductance and the arm resistance, respectively. Fig. 1(c) shows the topology of the 12P-DR, which comprises two six-pulse DRs (6P-DRs) in series. The ac-side currents of the two 6P-DRs are staggered by 30° through their link transformers, giving rise to 12 pulses per period in the dc-side current waveform of the 12P-DR.

B. Conventional Steady-State Analysis of the DR-MMC

In the steady-state analysis of the DR-MMC, the dc-link current i_{dc}, the ac-side current of the DR i_{DR}, the ac-side current of the MMC i_{MMC}, the dc-side voltage of the MMC $U_{\mathrm{dc,MMC}}$, as well as the internal electrical quantities of the MMC (including the modulation signal, the SM capacitor voltage u_{c}, and the arm current i_{arm}) need to be solved for according to the given active power of the wind farm P_{WF}, the PCC voltage u_{PCC}, and the dc-link voltage U_{dc0}.

Fig. 2 shows an equivalent circuit of the DR-MMC based HVdc transmission system [23], including the DRs, the MMC, the dc cables, and the inverter station. The two 12P-DRs are equated to a controlled voltage source in series with an equivalent reactance [25], where n_{DR} and $X_{\mathrm{T\_DR}}$ represent the turn ratio and the leakage reactance of DR transformers, respectively, and U_{PCC} denotes the peak value of the phase voltage at the PCC. Besides, R_{dc} is the resistance of the dc cables, and I_{dc} represents the dc-link current. Furthermore, the inverter station can be represented with a dc voltage source since the dc-link voltage of the HVdc transmission system is kept at constant U_{dc0} by the closed-loop control of the inverter station.

As shown in Fig. 2, when neglecting the power losses of the DR-MMC and the ripple of the dc-link current, the active power of the wind farm P_{WF} can be expressed as (1), which is used to calculate I_{dc} with known P_{WF} and U_{dc0} as

$$P_{\mathrm{WF}} = (U_{\mathrm{dc0}} + I_{\mathrm{dc}}R_{\mathrm{dc}})I_{\mathrm{dc}}. \tag{1}$$

In addition, the Kirchhoff's voltage law (KVL) equation for the circuit shown in Fig. 2 is given as follows, from which $U_{\mathrm{dc,MMC}}$ can be derived:

$$U_{\mathrm{dc,MMC}} + \frac{12\sqrt{3}n_{\mathrm{DR}}}{\pi}U_{\mathrm{PCC}} - \frac{12}{\pi}X_{\mathrm{T\_DR}}I_{\mathrm{dc}} = U_{\mathrm{dc0}} + R_{\mathrm{dc}}I_{\mathrm{dc}}. \tag{2}$$

When the effects of dc current ripple and ac-side ESR (including the transformer winding resistance and the diode on-resistance) are neglected, the overlap angle of the DR can be calculated approximately as follows [17], [24]:

$$\mu = \arccos\left(1 - \frac{2X_{\mathrm{T\_DR}}I_{\mathrm{dc}}}{\sqrt{3}n_{\mathrm{DR}}U_{\mathrm{PCC}}}\right). \tag{3}$$

Then, the amplitude and initial phase angle of i_{DR}'s fundamental frequency component can be obtained through FFT [17] as follows:

$$\begin{cases} I_{\mathrm{DR}} = \dfrac{3U_{\mathrm{PCC}}\sqrt{\sin^2(\mu) - 2\mu\sin(\mu)\cos(\mu) + \mu^2}}{2\pi n_{\mathrm{DR}}X_{\mathrm{T\_DR}}} \\ \varphi_{\mathrm{DR}} = \arctan\left(\dfrac{2\mu - \sin(2\mu)}{1 - \cos(2\mu)}\right) \end{cases}. \tag{4}$$

After calculating i_{DR}, the ac-side current of the MMC i_{MMC} can be obtained from the Kirchhoff's current law (KCL) equation at the PCC. Afterward, with the above-calculated I_{dc}, $U_{\mathrm{dc,MMC}}$, and i_{MMC}, and the known u_{PCC}, the internal electrical quantities of the MMC can be determined through the steady-state model of the individual MMC [11], [12], [13], [14], [15]. Up to now, the complete steady-state analysis of the DR-MMC has been done.

In the steady-state analysis of the DR-MMC presented in Fig. 2 and (1)–(4), the DR and MMC are treated as independent converters. In this way, the models of the DR and MMC are decoupled from each other, allowing all the electrical quantities of the DR and the external electrical quantities of the MMC to be expressed separately and analytically.

Nevertheless, as indicated in (3), the overlap angle of the DR is calculated using only the dc component of the dc-side current without considering the effect of the dc current ripple on the DR commutation process. Additionally, the equivalent circuit in Fig. 2 neglects the ac-side ESR, which turns out to be another important factor affecting the DR commutation process. If the above factors are taken into account, however, the overlap angle as well as the other electrical quantities can no longer be analytically expressed as (2)–(4), but has to be calculated numerically by iterative methods.

Moreover, the intercoupling between the DR and MMC is also neglected in the conventional DR-MMC models. This omission leads to considerable errors in calculating the electrical quantities of both the DR and MMC. If such intercoupling is taken into account, however, the conventional steady-state model, which is a simple addition of the DR and MMC models, becomes inapplicable, necessitating a new modeling approach.

III. Proposed Steady-State Model for the DR-MMC

Fig. 3 shows a novel equivalent circuit proposed by this article for the DR-MMC based HVdc transmission system. Considering the symmetry of the structure, Fig. 3 shows only half of the DR-MMC for simplicity. On the ac side of this equivalent circuit, L_{ac} represents the leakage inductance of the DR transformer, whereas R_{ac} denotes the ac-side ESR, including the winding resistance of transformers and the on-resistance of diodes. On the dc side of this equivalent circuit, L_{dc} represents the dc-side inductance, including the smoothing inductance and the line

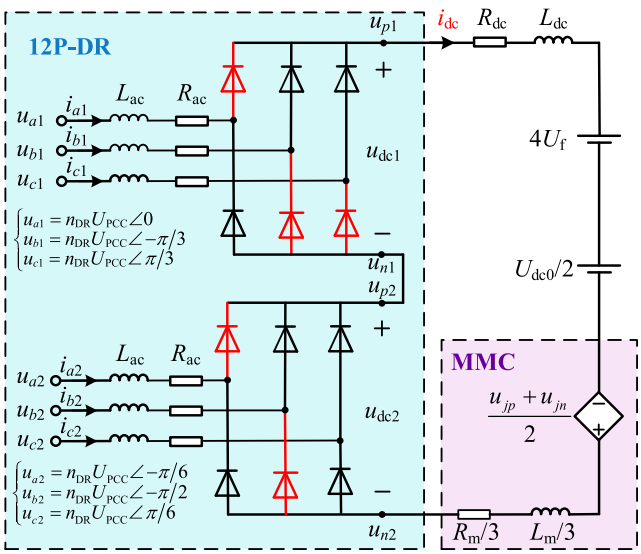

Fig. 3. Proposed equivalent circuit of the DR-MMC.

inductance; U_f is the voltage drop of the diode; and u_{jp} and u_{jn} denote the upper and lower arm voltages of phase j ($j = a, b, c$), respectively. The dc side of the MMC is equated to a series connection of $(u_{jp} + u_{jn})/2$, one-third arm inductance, and one-third arm resistance.

Unlike the equivalent circuit in Fig. 2, which only considers the dc component of i_{dc}, the proposed equivalent circuit incorporates all components of i_{dc}. Additionally, the ac-side ESR (R_{ac}) and the coupling from the MMC are also taken into account. This equivalent circuit will be employed in the analysis of the DR commutation process and the development of the DR-MMC's steady-state model subsequently.

A. More Elaborate Description of the DR Commutation Process

Section II has pointed out that the conventional steady-state analysis method could lead to considerable errors in calculating the overlap angle. The commutation process of the DR will be analyzed in detail below to obtain an accurate value of μ.

Fig. 4(a) and (b) shows the waveforms of the ac-side voltages, the ac-side currents, and the dc-side current of two 6P-DRs when $\mu \le \pi/6$ and $\mu > \pi/6$, respectively. As shown in Fig. 3, the physical meaning of the overlap angle μ is the electrical angle at which the commutation process continues.

In this article, the waveforms in the first $\pi/3$ period will be analyzed. It can be seen from Fig. 4 that whether $\mu \le \pi/6$ or $\mu > \pi/6$, the operating modes of the 12P-DR can be divided into four stages (a, b, c, and d) according to whether each individual 6P-DR is in the commutating or the conducting interval.

When $\mu \le \pi/6$, the differential equations with regard to i_{dc} can be derived, as presented in (5) shown at the bottom of this page. The detailed derivation process is given in the Appendix. The phase voltages of the DR (u_{a1}, u_{b1}, and u_{c1} and u_{a2}, u_{b2}, u_{c2}) have already been shown in Fig. 4.

The dc-link current at $\omega t = 0$ is set as $I_{dc,t0}$, whereas that at $\omega t = \mu$ is set as $I_{dc,min}$, as shown in Fig. 4. The initial conditions for the differential equations in (5), can be expressed as

$$\begin{cases} i_{dc}(0) = i_{dc}(\pi/6) = I_{dc,t0} \\ i_{dc}(\mu) = i_{dc}(\mu) = I_{dc,min} \end{cases}. \tag{6}$$

Combining (5) and (6), the waveform $i_{dc}(\omega t)$ in 0–π/6 can be solved. Since the dc-link current has a period of π/6, $i_{dc}(\omega t)$ can be obtained across the entire time range. The only unknown in the expression of $i_{dc}(\omega t)$ is the overlap angle μ when $u_{jp} + u_{jn}$ in (5) is known.

Similarly, when $\mu > \pi/6$, the differential equation and the corresponding initial conditions can also be derived, as shown in (7) and (8), from which $i_{dc}(\omega t)$ across the entire time range can be obtained as well. Therein, (7) is shown at the bottom of this page.

$$\begin{cases} i_{dc}(0) = i_{dc}(\pi/6) = I_{dc,t0} \\ i_{dc}(\mu - \pi/6) = i_{dc}(\mu - \pi/6) = I_{dc,min} \end{cases}. \tag{8}$$

Next, by combining (21) and (22) in the Appendix, the differential equation with regard to i_{b1} during 0–μ can be derived, as follows:

$$\begin{cases} \frac{di_{b1}}{dt} = -\frac{1}{2}\frac{di_{dc}}{dt} - \frac{R_{ac}}{L_{ac}}i_{b1} - \frac{R_{ac}}{L_{ac}}i_{dc} + \frac{u_{b1}-u_{c1}}{2L_{ac}} \\ i_{b1}(0) = -i_{dc}(0) \end{cases}. \tag{9}$$

The waveform $i_{b1}(\omega t)$ during 0–μ can be obtained by solving (9). Similarly, the only unknown variable in the expression is μ. According to the physical meaning of the overlap angle, a nonlinear equation $i_{b1}(\mu) = 0$ is obtained, from which an accurate value of μ can be solved.

After substituting the obtained μ into (5)–(8), the complete waveform $i_{dc}(\omega t)$ can be derived, followed by the expressions of the ac-side current of the DR given as (10) shown at the bottom of the next page.

So far, a more elaborate description of the DR commutation process has been completed. The work done in this subsection

$$\begin{cases} \left(L_{dc} + \frac{L_m}{3} + 3.5L_{ac}\right)\frac{di_{dc}}{dt} = -\left(R_{dc} + \frac{R_m}{3} + 3.5R_{ac}\right)i_{dc} + 1.5u_{a1} + u_{a2} - u_{b2} - \left(4U_f + \frac{U_{dc0}}{2} - \frac{u_{jp}+u_{jn}}{2}\right), 0 \le \omega t \le \mu \\ \left(L_{dc} + \frac{L_m}{3} + 4L_{ac}\right)\frac{di_{dc}}{dt} = -\left(R_{dc} + \frac{R_m}{3} + 4R_{ac}\right)i_{dc} + u_{a1} - u_{c1} + u_{a2} - u_{b2} - \left(4U_f + \frac{U_{dc0}}{2} - \frac{u_{jp}+u_{jn}}{2}\right), \mu < \omega t \le \pi/6 \end{cases} \tag{5}$$

$$\begin{cases} \left(L_{dc} + \frac{L_m}{3} + 3L_{ac}\right)\frac{di_{dc}}{dt} = -\left(R_{dc} + \frac{R_m}{3} + 3R_{ac}\right)i_{dc} + 1.5u_{a1} - 1.5u_{b2} - \left(4U_f + \frac{U_{dc0}}{2} - \frac{u_{jp}+u_{jn}}{2}\right), 0 \le \omega t \le \mu \\ \left(L_{dc} + \frac{L_m}{3} + 3.5L_{ac}\right)\frac{di_{dc}}{dt} = -\left(R_{dc} + \frac{R_m}{3} + 3.5R_{ac}\right)i_{dc} + 1.5u_{a1} + u_{a2} - u_{b2} - \left(4U_f + \frac{U_{dc0}}{2} - \frac{u_{jp}+u_{jn}}{2}\right), \mu < \omega t \le \pi/6 \end{cases} \tag{7}$$

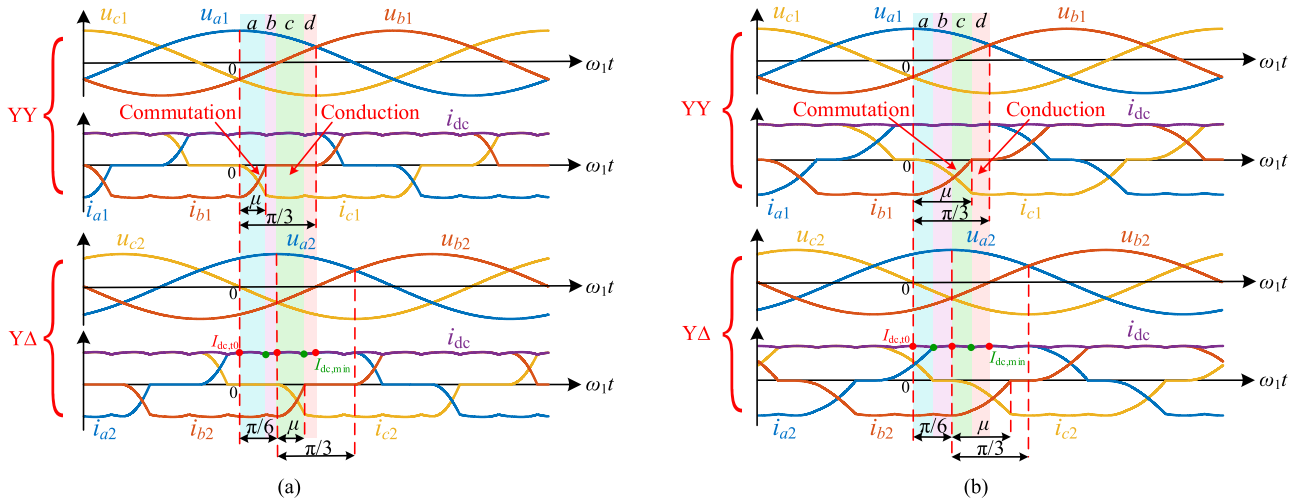

Fig. 4. Waveforms of the AC-side voltages, AC-side currents, and DC-side current of the 12P-DR. (a) When $\mu \leq \pi/6$. (b) When $\mu > \pi/6$.

serves as an important part of the subsequent steady-state model of the DR-MMC, facilitating a more accurate steady-state analysis of this hybrid topology.

B. Steady-State Model Constituted by Double Loops

Fig. 5 shows the proposed steady-state model constituted by double loops. In the upper half of Fig. 5, the commutation process of the DR and the power conservation of this hybrid topology together form the outer loop. This loop is utilized to solve for all the electrical quantities of the DR and the external electrical quantities of the MMC (including the dc-side voltage $u_{\mathrm{dc,MMC}}$ and the ac-side current i_{MMC}). In the lower half of Fig. 5, the steady-state of the individual MMC serves as the inner loop, to solve for the MMC's internal electrical quantities based on its external electrical quantities. The iterative procedure in the outer and inner loops will be detailed in the following.

1) Outer Loop: According to the power conservation law, the total ac-side power of the DR-MMC is equal to the sum of its dc-side power and the power losses (including the losses of the transformer winding resistance, diodes, and MMC arm resistance), accordingly

$$P_{\mathrm{WF}} = U_{\mathrm{dc0}} I_{\mathrm{dc}} + 4 \cdot 3 R_{\mathrm{ac}} I_{\mathrm{DR,rms}}^2 + 4 \cdot 2 U_f I_{\mathrm{dc}} + \frac{3}{2} R_{\mathrm{eq}} \left(I_{\mathrm{MMC}} / n_{\mathrm{MMC}} \right)^2 + \left(\frac{2}{3} R_{\mathrm{m}} + 2 R_{\mathrm{dc}} \right) I_{\mathrm{dc}}^2 \quad (11)$$

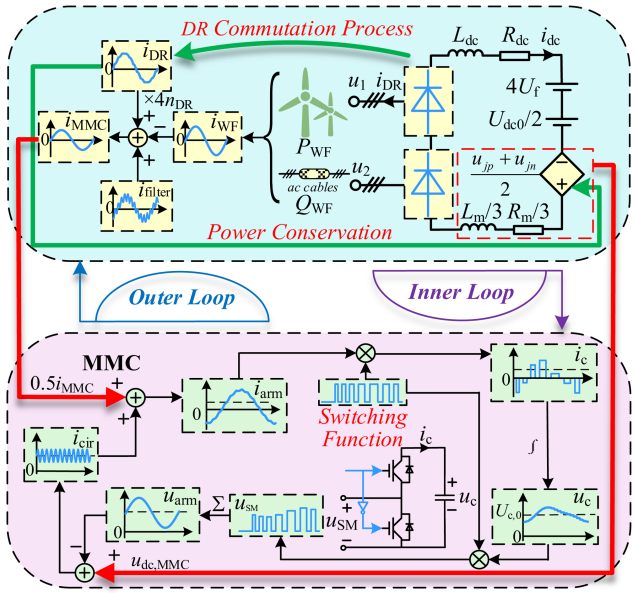

Fig. 5. Illustration of the proposed steady-state model constituted by double loops.

where R_{eq} is equal to half of the MMC arm resistance plus the transformer winding resistance, n_{MMC} denotes the turn ratio of the MMC transformer, and I_{MMC} represents the amplitude of i_{MMC}.

$$\begin{cases} i_{a1} = i_{\mathrm{dc}}, & 0 < \omega t \leq \pi/3 \\ \frac{di_{a1}}{dt} + \frac{R_{\mathrm{ac}}}{L_{\mathrm{ac}}} i_{a1} = \frac{1}{2}\frac{di_{\mathrm{dc}}}{dt} + \frac{R_{\mathrm{ac}}}{2L_{\mathrm{ac}}} i_{\mathrm{dc}} + \frac{u_{a1}-u_{b1}}{2L_{\mathrm{ac}}}, i_{a1}(\pi/3) = i_{\mathrm{dc}}(0), & \pi/3 < \omega t \leq \mu + \pi/3 \\ i_{a1} = 0, & \mu + \pi/3 < \omega t \leq 2\pi/3 \\ \frac{di_{a1}}{dt} + \frac{R_{\mathrm{ac}}}{L_{\mathrm{ac}}} i_{a1} = -\frac{1}{2}\frac{di_{\mathrm{dc}}}{dt} - \frac{R_{\mathrm{ac}}}{2L_{\mathrm{ac}}} i_{\mathrm{dc}} + \frac{u_{a1}-u_{c1}}{2L_{\mathrm{ac}}}, i_{a1}(2\pi/3) = 0, & 2\pi/3 < \omega t \leq 2\pi/3 + \mu \\ i_{a1} = -i_{\mathrm{dc}}, & 2\pi/3 + \mu < \omega t \leq \pi \\ i_{a1} = -i_{a1}(\omega t - \pi), & \pi < \omega t \leq 2\pi \end{cases} \quad (10)$$

Besides, the power conservation equation for the equivalent circuit shown in Fig. 3 can be written as

$$2\cdot\frac{3}{2}U_{\mathrm{PCC}}n_{\mathrm{DR}}I_{\mathrm{DR}}\cos\left(\varphi_{\mathrm{DR}}\right)=\left(4U_f+\frac{U_{\mathrm{dc0}}}{2}-\frac{u_{jp}+u_{jn}}{2}\right)I_{\mathrm{dc}}+2\cdot3I_{\mathrm{DR,rms}}^2R_{\mathrm{ac}}+\left(\frac{1}{3}R_{\mathrm{m}}+R_{\mathrm{dc}}\right)I_{\mathrm{dc}}^2 \tag{12}$$

where I_{DR} and φ_{DR} represent the amplitude and the phase angle of the fundamental component of i_{DR}, respectively; $I_{\mathrm{DR,rms}}$ denotes the root mean square (RMS) value of i_{DR}, and I_{dc} can be solved by (11). Equation (12) can be utilized to calculate $u_{jp}+u_{jn}$ on the condition that i_{DR} is known.

Moreover, the DR commutation process established in Section III-A can derive i_{DR} on the condition that $u_{jp}+u_{jn}$ is known. In this way, the accurate DR commutation process and the power conservation equations composed of (11) and (12) make up a loop, as shown in the outer loop in Fig. 5. Thus, from any value of $u_{jp}+u_{jn}$, this outer loop can calculate a new value of $u_{jp}+u_{jn}$, which is denoted as $f(u_{jp}+u_{jn})$. The numerical solution of $u_{jp}+u_{jn}$ can be obtained by solving the nonlinear equation $f(u_{jp}+u_{jn})=u_{jp}+u_{jn}$, whereafter the numerical solutions of i_{DR} and i_{dc} can be obtained according to the established DR model. The MATLAB function "*fsolve*" or the Newton iteration method [26] can be employed to solve the nonlinear equation.

Afterward, it is also required to obtain the external electrical quantities of the MMC (including $u_{\mathrm{dc,MMC}}$ and i_{MMC}), to calculate its internal electrical quantities through the inner loop subsequently. Among them, $u_{\mathrm{dc,MMC}}$ can be expressed as [27]

$$\frac{u_{\mathrm{dc,MMC}}}{2}=\frac{u_{jp}+u_{jn}}{2}+R_{\mathrm{m}}i_{\mathrm{cir}j}+L_{\mathrm{m}}\frac{di_{\mathrm{cir}j}}{dt} \tag{13}$$

where $i_{\mathrm{cir}j}$ is the circulating current. Therein, the second-order component of $i_{\mathrm{cir}j}$ are generally suppressed by circulating current suppression control (CCSC) [28]. Thus, $i_{\mathrm{cir}j}$ can be substituted by $I_{\mathrm{dc}}/3$ in the calculation of $U_{\mathrm{dc,MMC}}$.

As for the calculation of i_{MMC}, the KCL equation at the PCC can be listed as

$$i_{\mathrm{MMC}}=-(i_{\mathrm{WF}}-4n_{\mathrm{DR}}i_{\mathrm{DR}}-i_{\mathrm{filter}}) \tag{14}$$

where i_{WF} is the wind farm current, which can be calculated from the known wind farm power P_{WF}, the transmission line impedance, and U_{PCC}. i_{filter} is the ac-side filter current, which can be derived from the filter impedance and U_{PCC}.

2) Inner Loop: The dc-side voltage and the ac-side current of the MMC have been obtained from the iterative calculation of the above outer loop, and the ac-side voltage of the MMC, i.e., the PCC voltage, is known. Building upon that, the internal electrical quantities of the MMC, including the modulation signal, the arm current, and the SM capacitor voltage, can be calculated through the inner loop, that is, the steady-state models of the individual MMC. Taking phase-*a* as an example, the inner loop can be detailed below.

Firstly, the circulating current i_{cir} is assumed to be unknown, and the arm current i_{arm} can be calculated by superimposing i_{cir} and known i_{MMC}, as shown in the following equation:

$$\begin{cases}i_{ap}(t)=i_{\mathrm{cir}}(t)+i_{\mathrm{MMC}}(t)/2\\ i_{an}(t)=i_{\mathrm{cir}}(t)-i_{\mathrm{MMC}}(t)/2\end{cases} \tag{15}$$

where i_{ap} and i_{an} represent the upper and lower arm currents, respectively.

Next, the product of i_{arm} and the switching function contributes to the SM capacitor current i_{c} is shown in the following equation:

$$\begin{cases}i_{c,ap}(t)=m_{ap}(t)\cdot i_{ap}(t)\\ i_{c,an}(t)=m_{an}(t)\cdot i_{an}(t)\end{cases} \tag{16}$$

where the modulation signal m_{ap}, which is equal to the averaged switching functions. The SM capacitor voltage u_c can be expressed by integrating the SM capacitor current i_c, as shown in the following equation:

$$\begin{cases}u_{c,ap}(t)=U_{c,0}+\frac{1}{C_{\mathrm{SM}}}\int i_{c,ap}(t)dt\\ u_{c,an}(t)=U_{c,0}+\frac{1}{C_{\mathrm{SM}}}\int i_{c,an}(t)dt\end{cases} \tag{17}$$

where $U_{c,0}$ denotes the dc component of the SM capacitor voltage and C_{SM} represents the SM capacitance.

Then, the product of u_c and the switching function contributes to the SM voltage u_{SM}, which is summed to get the arm voltage u_{arm}

$$\begin{cases}u_{ap}(t)=N\cdot m_{ap}(t)\cdot u_{c,ap}(t)\\ u_{an}(t)=N\cdot m_{an}(t)\cdot u_{c,an}(t)\end{cases} \tag{18}$$

Afterward, a new value of i_{cir} can be obtained by substituting u_{arm} and known $u_{\mathrm{dc,MMC}}$ into (13).

Besides, the inner electromotive force of phase *a* can be expressed as $(u_{an}-u_{ap})/2$, which can also be derived from transmitted active and reactive powers (P_{MMC} and Q_{MMC})

$$\frac{u_{an}(t)-u_{ap}(t)}{2}=\frac{\sqrt{a^2+b^2}}{3n_{\mathrm{MMC}}U_{\mathrm{PCC}}/\sqrt{2}}\sin\left(\omega t-\arctan\left(\frac{a}{b}\right)\right) \tag{19}$$

where $a=P_{\mathrm{MMC}}X_{\mathrm{eq}}$ and $b=3n_{\mathrm{MMC}}^2U_{\mathrm{PCC}}^2-Q_{\mathrm{MMC}}X_{\mathrm{eq}}$, X_{eq} is equal to half of the MMC arm reactance plus the transformer leakage reactance. Therein, P_{MMC} and Q_{MMC} can be calculated by the known U_{PCC} and the derived i_{MMC} from the outer loop.

In this way, the internal electrical quantities of the MMC make up the inner loop as shown in Fig. 5. The time-varying variables in (13) and (15)–(19) are then expressed by their respective multiple frequency components to establish a system of nonlinear equations, by solving which all the internal electrical quantities of the MMC can be derived.

So far, the complete DR-MMC modeling has been accomplished. The model established in this section is a completely novel model. Unlike conventional models that calculate the overlap angle using only the dc component of the dc-side current, the proposed model solves for the accurate overlap angle through an iterative method, based on a more elaborate description of the DR commutation process within the DR-MMC. Moreover, unlike conventional models that are a simple addition of the DR and MMC models, the established model is constituted by

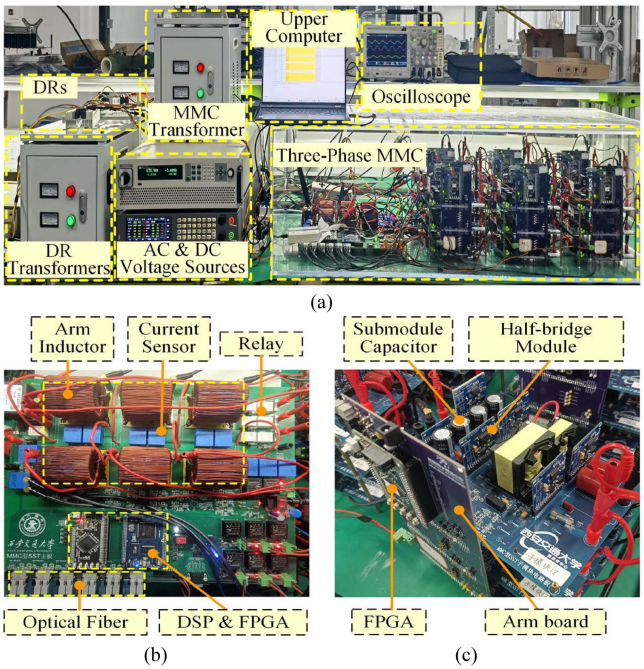

Fig. 6. Experimental platform of the DR-MMC prototype. (a) Overall platform. (b) Main board of the MMC. (c) Arm board and submodule board of the MMC.

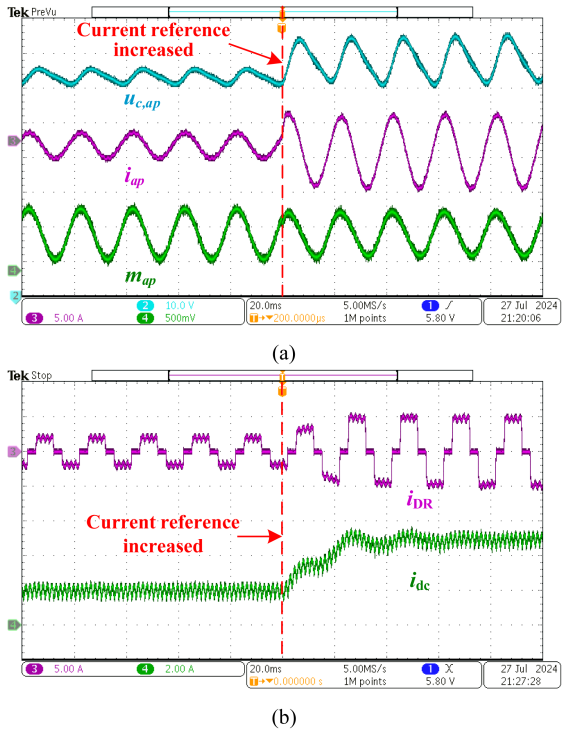

Fig. 7. Transient waveforms after the *d*-axis current reference increased. (a) Waveforms of the SM capacitor voltage, arm current, and modulation signal. (b) Waveforms of the DC-link current and the DR's AC-side current.

double loops. This structure allows for a thorough consideration of the intercoupling between the DR and MMC, thereby enabling accurate calculations of all electrical quantities within this hybrid topology. Moreover, in the proposed double-loop structure, the calculation of the MMC's internal electrical quantities can be separated from the overall DR-MMC model, which significantly simplifies both the programming and calculation.

IV. Experimental Verification

A. Introduction of the Experimental Platform

A scaled-down DR-MMC prototype was constructed to verify the effectiveness and accuracy of the proposed steady-state model. Fig. 6(a) shows the photograph of the overall platform, which consists of one MMC, two DRs, and three transformers. The dc ports of the DRs and MMC are connected in series and then to a bidirectional dc source, whereas their ac ports are connected to the same three-phase ac source through their respective transformers. An upper computer is employed for real-time data reception, status display, and to issue control commands to the DR-MMC system. The main circuit parameters of this prototype are listed in Table I.

The MMC's control structure primarily includes SM balancing control [29], ac current control, and CCSC, with phase-shifted carrier modulation [12] at a 10-kHz switching frequency. Regarding the controller system, as shown in Fig. 6(b), a DSP (TMS320F28335) and an field-programmable gate array (FPGA) (EP4CE10E22) together serve as master controllers where control strategies are implemented. Meanwhile, as shown in Fig. 6(c), each arm is equipped with an FPGA as the slave controller to collect SM capacitor voltages and generate half-bridge driving signals. The communication between the master and slave controllers occurs via optical fibers.

TABLE I
Main Circuit Parameters of the DR-MMC Prototype

	Parameter	Symbol	Value
System	Rated wind farm power	P_{WF}	3.5 kW
	Fundamental frequency	ω	314 rad/s
	Rated dc-link voltage	U_{dc0}	±320 V
	PCC voltage	U_{PCC}	380 V
12P-DR	Transformer turn ratio	n_{DR}	380 V/170 V
	Leakage inductance	L_{T_DR}	2.5 mH
	Leakage resistance	R_{T_DR}	1.35 Ω
	Rated capacity	S_{DR}	1800 VA
	Rated dc-side voltage	$U_{dc,DR}$	215 V
	Forward voltage of diodes	U_f	0.72 V
	On-resistance of diodes	R_{on}	0.01 Ω
MMC	Transformer turn ratio	n_{MMC}	380 V/90 V
	Leakage inductance	L_{T_MMC}	2.2 mH
	Leakage resistance	R_{T_MMC}	0.58 Ω
	Rated capacity	S_{MMC}	1680 VA
	Rated dc-side voltage	$U_{dc,MMCN}$	210 V
	Number of SMs per arm	N	3
	Submodule capacitance	C_{sm}	1080 μF
	Arm inductance	L_m	5 mH
	Arm resistance	R_m	0.6 Ω

The active power transmitted by the DR-MMC is increased by raising the MMC's *d*-axis current reference in this experiment. The sudden increase in this current reference induces dynamic responses in the electrical quantities of the DR-MMC, as depicted in Fig. 7. Specifically, Fig. 7(a) shows the variations in

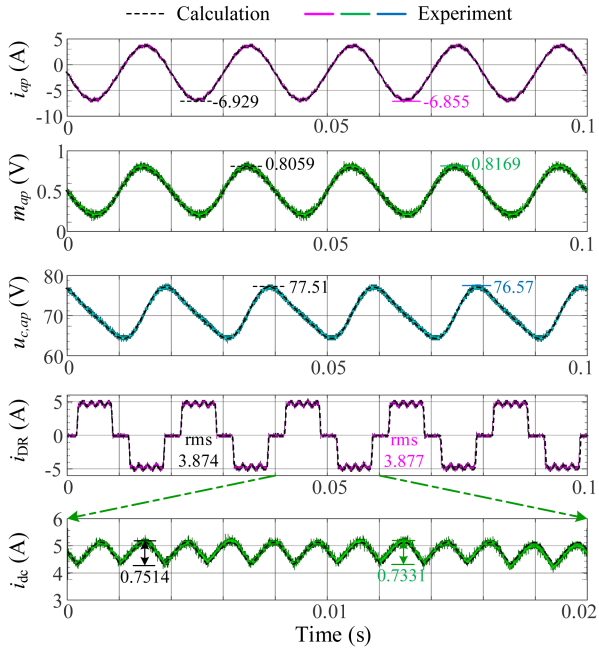

Fig. 8. Comparison between calculation results and experimental waveforms when $P_{\mathrm{WF}} = 1.0$ p.u.

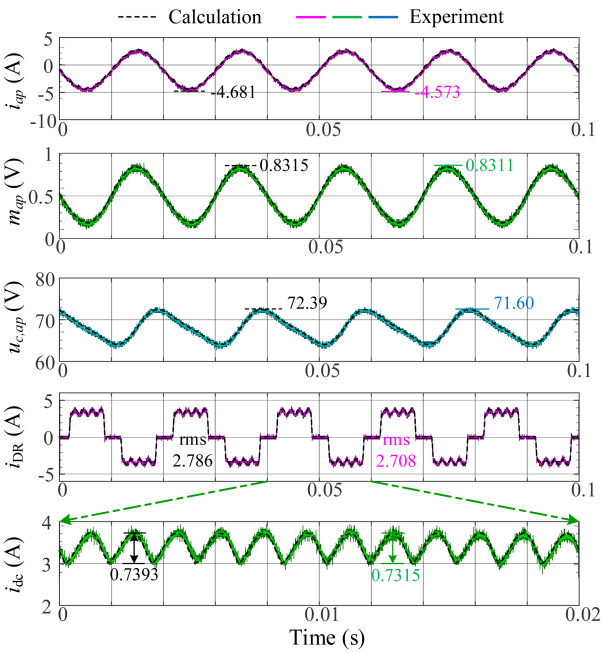

Fig. 9. Comparison between calculation results and experimental waveforms when $P_{\mathrm{WF}} = 0.7$ p.u.

the SM capacitor voltage, arm current, and modulation signal of the MMC, whereas Fig. 7(b) presents the changes in the ac-side current of the DR and the dc-link current. The results indicate that the waveforms of both the MMC and DR remain stable and quickly reach a new steady state. These responses confirm the effectiveness of the experimental platform and control system, supporting further validation of the proposed steady-state model.

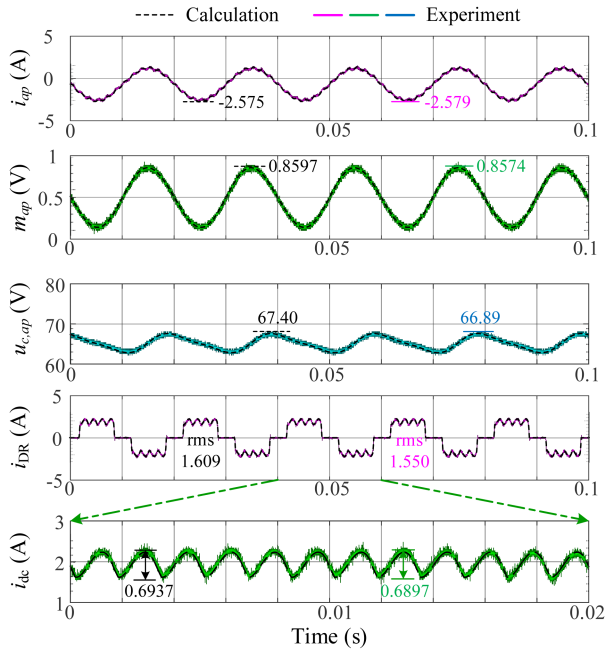

Fig. 10. Comparison between calculation results and experimental waveforms when $P_{\mathrm{WF}} = 0.4$ p.u.

B. Verification of Accuracy

Figs. 8–10 present comparisons between the calculated results and experimental waveforms under three typical operating conditions. In these figures, the active power is expressed in per-unit values, with the rated power of the DR-MMC as the power base. The calculated results are indicated by black dashed lines, whereas the experimental waveforms are presented as colored solid lines. Each figure displays five electrical quantities in the following sequence from top to bottom: upper-arm current i_{ap}, modulation signal m_{ap}, SM capacitor voltage $u_{\mathrm{c},ap}$, DR's ac-side current i_{DR}, and dc-link current i_{dc}. As evident in these figures, the calculated results closely align with the experimental waveforms, confirming that the proposed model achieves sufficiently high accuracy.

To quantify the error of the proposed model more intuitively, Tables II–IV simultaneously present the simulated, experimental, and calculated results of key electrical quantities under three typical operating conditions. These tables include the peak value of the modulation signal, the arm current, as well as the SM capacitor voltage, the RMS value of the DR's ac-side current, the dc and ripple components of the dc-link current, and the MMC's dc-side voltage. Additionally, the errors between the calculations and simulated/experimental results are listed as well for both the proposed and conventional models. As demonstrated in Tables II–IV, there is a high degree of agreement between the simulated/experimental results and the calculation results derived from the proposed model. In contrast, the calculations obtained from the conventional model exhibit significant deviations from these results, highlighting the enhanced accuracy provided by the proposed model.

TABLE II
COMPARISONS BETWEEN THE SIMULATED, EXPERIMENTAL, AND CALCULATED RESULTS WHEN $P_{\mathrm{WF}} = 1.0$ P.U.

Electrical quantities	Measured results		Proposed model			Conventional model		
	Simulation	Experiment	Calculation	vs simulation	vs experiment	Calculation	vs simulation	vs experiment
m_{peak}	0.8064	0.8169	0.8059	0.06%	1.35%	0.8580	6.40%	5.03%
$I_{\mathrm{arm,peak}}$ (A)	6.917	6.855	6.929	0.17%	1.08%	6.074	12.2%	11.4%
$U_{c,\mathrm{peak}}$ (V)	77.50	76.57	77.51	0.01%	1.23%	66.50	14.2%	13.2%
$I_{\mathrm{DR,rms}}$ (A)	3.873	3.877	3.874	0.03%	0.08%	4.235	9.35%	9.23%
I_{dc} (A)	4.773	4.801	4.772	0.02%	0.60%	5.226	9.49%	8.85%
Δi_{dc} (A)	0.7450	0.7331	0.7514	0.86%	2.50%	Ignored	100%	100%
$U_{\mathrm{dc,MMC}}$ (V)	210.3	209.6	210.4	0.05%	0.38%	182.4	13.3%	13.0%

TABLE III
COMPARISONS BETWEEN THE SIMULATED, EXPERIMENTAL, AND CALCULATED RESULTS WHEN $P_{\mathrm{WF}} = 0.7$ P.U.

Electrical quantities	Measured results		Proposed model			Conventional model		
	Simulation	Experiment	Calculation	vs simulation	vs experiment	Calculation	vs simulation	vs experiment
m_{peak}	0.8318	0.8311	0.8315	0.04%	0.05%	0.8726	4.91%	4.99%
$I_{\mathrm{arm,peak}}$ (A)	4.673	4.573	4.681	0.17%	2.36%	4.217	9.76%	7.78%
$U_{c,\mathrm{peak}}$ (V)	72.39	71.60	72.39	0.00%	1.10%	64.57	10.8%	9.82%
$I_{\mathrm{DR,rms}}$ (A)	2.783	2.708	2.786	0.11%	2.88%	2.952	6.07%	9.01%
I_{dc} (A)	3.419	3.408	3.422	0.09%	0.41%	3.638	6.41%	6.75%
Δi_{dc} (A)	0.7357	0.7315	0.7393	0.49%	1.07%	Ignored	100%	100%
$U_{\mathrm{dc,MMC}}$ (V)	202.9	202.6	202.9	0.00%	0.15%	181.9	10.3%	10.2%

TABLE IV
COMPARISONS BETWEEN THE SIMULATED, EXPERIMENTAL, AND CALCULATED RESULTS WHEN $P_{\mathrm{WF}} = 0.4$ P.U.

Electrical quantities	Measured results		Proposed model			Conventional model		
	Simulation	Experiment	Calculation	vs simulation	vs experiment	Calculation	vs simulation	vs experiment
m_{peak}	0.8599	0.8574	0.8597	0.02%	0.27%	0.8874	3.20%	3.50%
$I_{\mathrm{arm,peak}}$ (A)	2.571	2.579	2.575	0.16%	0.16%	2.359	8.25%	8.53%
$U_{c,\mathrm{peak}}$ (V)	67.40	66.89	67.40	0.00%	0.76%	62.67	7.02%	6.31%
$I_{\mathrm{DR,rms}}$ (A)	1.613	1.550	1.609	0.25%	3.81%	1.658	2.79%	6.97%
I_{dc} (A)	1.968	1.956	1.970	0.10%	0.72%	2.040	3.66%	4.29%
Δi_{dc} (A)	0.6966	0.6897	0.6937	0.42%	0.58%	Ignored	100%	100%
$U_{\mathrm{dc,MMC}}$ (V)	194.8	195.1	194.8	0.00%	0.15%	181.5	6.83%	6.97%

C. Evaluation of the Impacts of Additional Factors

The factors considered by the proposed model beyond those in conventional models include the dc current ripple, the ac-side ESR, and the intercoupling between the DR and MMC. The impacts of these additional factors on model accuracy are evaluated in the following.

For the DR, the coupling from the MMC primarily arises from the arm inductance, which, along with the smoothing inductance, determines the dc current ripple. As shown in Fig. 11, the dc current ripple increases with the decrease of the dc-side equivalent series inductance (ESL), which is defined as the sum of the smoothing inductance and two-thirds of the arm inductance. As indicated in (9), this ripple affects the commutation process of the DR. Consequently, the maximum calculation errors of the conventional model for both the overlap angle μ and the RMS value of the DR's ac-side current $I_{\mathrm{DR,rms}}$ increases with the decrease of the ESL, as indicated in Fig. 11. These observations confirm that the dc current ripple as well as the coupling from the MMC cannot be neglected for accurately determining the DR's electrical quantities.

Moreover, Fig. 11 also indicates that the maximum error in the peak value of the MMC's arm current increases as the ESL decreases. This owes to the fact that the dc current ripple generated by twelve-pulse DRs introduces same-frequency components into the MMC's circulating current. This observation confirms that the coupling from the DR cannot be neglected for accurately determining the MMC's electrical quantities.

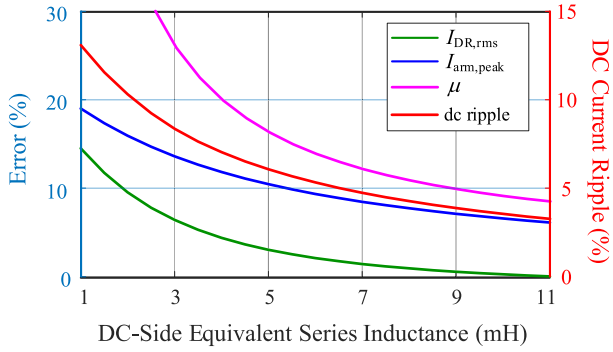

Fig. 11. Impacts of the DC current ripple on the maximum calculation errors of $I_{\mathrm{DR,rms}}$, $I_{\mathrm{arm,peak}}$, and μ.

Next, the impact of the ac-side ESR on the model accuracy is evaluated. Fig. 12 shows how the maximum calculation errors

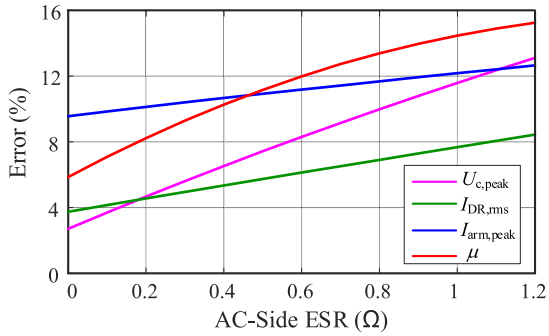

Fig. 12. Impacts of the AC-side ESR on the maximum calculation errors of $U_{\mathrm{c,peak}}$, $I_{\mathrm{DR,rms}}$, $I_{\mathrm{arm,peak}}$, and μ.

for a few electrical quantities vary with the ac-side ESR. In this figure, the ac-side ESR ranges from 0 to 2 Ω, corresponding to a drop in the efficiency of the DR transformer from 100% to 95%. Notably, the maximum errors for both μ and $I_{\mathrm{DR,rms}}$ increase significantly with the ac-side ESR. This implies that the ac-side ESR substantially affects the DR's commutation process and electrical quantities. Furthermore, the MMC's electrical quantities $I_{\mathrm{arm,peak}}$ and $U_{\mathrm{c,peak}}$ are also affected due to the intercoupling between the DR and MMC.

V. Conclusion

This article focuses on the establishment of an improved steady-state model for the DR-MMC. The conclusions can be drawn as follows.

1) The inability of existing steady-state analysis methods to accurately determine electrical quantities attributes to their neglect of the effect of the dc current ripple and ac-side ESR on the DR commutation process, as well as the oversight of the intercoupling between the DR and MMC. The proposed model, which is based on an elaborate description of the DR commutation process and constituted by double loops, specifically addresses these limitations.
2) The experimental waveforms from a scaled-down prototype are closely aligned with the calculated results form the proposed model, but exhibit considerable discrepancies when compared to the results derived from the conventional model. This disparity confirms the enhanced accuracy provided by the proposed model.
3) The evaluation of the impacts of the additional factors considered by the proposed model, beyond those in conventional models, confirms that all these factors are non-negligible for accurately determining the electrical quantities of the DR-MMC.

The work done in this article seeks to provide a comprehensive steady-state analysis method for the DR-MMC based hybrid topology used in offshore wind power transmission. The proposed method can offer accurate references for the circuit parameter design, power device selection, and operation performance evaluation of the DR-MMC, thereby facilitating the economical design and safe operation of this hybrid topology.

Appendix

The differential equation for the dc-link current i_{dc} during the time interval of 0–$\pi/6$ will be derived below.

According to Fig. 3, the KVL equation for the dc side of the equivalent circuit can be listed as

$$\left(R_{\mathrm{dc}}+\frac{R_{\mathrm{m}}}{3}\right)i_{\mathrm{dc}}+\left(L_{\mathrm{dc}}+\frac{L_{\mathrm{m}}}{3}\right)\frac{di_{\mathrm{dc}}}{dt} = u_{\mathrm{dc1}}+u_{\mathrm{dc2}}-\left(4U_{\mathrm{f}}+\frac{U_{\mathrm{dc0}}}{2}-\frac{u_{jp}+u_{jn}}{2}\right) \tag{20}$$

where u_{dc1} and u_{dc2} are the dc-side voltages of two 6P-DRs. It can be seen from (20) that to obtain the differential equation of i_{dc}, the expression of $u_{\mathrm{dc1}}+u_{\mathrm{dc2}}$ must be obtained first.

When $0\le\omega t<\mu$, as indicated in Fig. 4, for the 6P-DR connected by the Y-Y transformer, the upper diode in phase a is in the ON state, whereas the lower ones in both phase b and c are in the commutating state. Therefore, according to Fig. 3, KVL and KCL equations can be listed in the following equations:

$$\begin{cases} L_{\mathrm{ac}}\frac{di_{a1}}{dt}=-R_{\mathrm{ac}}i_{a1}+u_{a1}-u_{p1} \\ L_{\mathrm{ac}}\frac{di_{b1}}{dt}=-R_{\mathrm{ac}}i_{b1}+u_{b1}-u_{n1} \\ L_{\mathrm{ac}}\frac{di_{c1}}{dt}=-R_{\mathrm{ac}}i_{c1}+u_{c1}-u_{n1} \end{cases} \tag{21}$$

$$\begin{cases} i_{a1}=i_{\mathrm{dc}} \\ i_{b1}+i_{c1}=-i_{\mathrm{dc}} \end{cases} \tag{22}$$

where u_{p1} and u_{n1} denote the potentials of the positive and negative poles on the dc side of the 6P-DR, respectively.

In addition, when $\mu\le\omega t<\pi/3$, the upper diode in phase a and the lower diode in phase c are in the ON state, whereas phase b is in the cutoff state, accordingly

$$\begin{cases} L_{\mathrm{ac}}\frac{di_{a1}}{dt}=-R_{\mathrm{ac}}i_{a1}+u_{a1}-u_{p1} \\ L_{\mathrm{ac}}\frac{di_{c1}}{dt}=-R_{\mathrm{ac}}i_{c1}+u_{c1}-u_{n1} \end{cases} \tag{23}$$

$$\begin{cases} i_{a1}=i_{\mathrm{dc}} \\ i_{c1}=-i_{\mathrm{dc}} \\ i_{b1}=0 \end{cases}. \tag{24}$$

Combing (21)–(24), the dc-side voltage of the 6P-DR connected by the Y-Y transformer can be expressed as

$$u_{\mathrm{dc1}}=u_{p1}-u_{n1} = \begin{cases} -\frac{3R_{\mathrm{ac}}}{2}i_{\mathrm{dc}}-\frac{3L_{\mathrm{ac}}}{2}\frac{di_{\mathrm{dc}}}{dt}+\frac{3}{2}u_{a1} & 0\le\omega t\le\mu \\ -2R_{\mathrm{ac}}i_{\mathrm{dc}}-2L_{\mathrm{ac}}\frac{di_{\mathrm{dc}}}{dt}+u_{a1}-u_{c1} & \mu\le\omega t\le\pi/3 \end{cases} \tag{25}$$

Similarly, the dc-side voltage of the 6P-DR that is connected by the Y-Δ transformer can be derived, and the detail expression is related to the range of μ. More specifically, when $\mu\le\pi/6$, u_{dc2}

can be expressed as follows:

$$\begin{cases} u_{\mathrm{dc}2} = -2R_{\mathrm{ac}}i_{\mathrm{dc}} - 2L_{\mathrm{ac}}\frac{di_{\mathrm{dc}}}{dt} + u_{a2} - u_{b2}, 0 \le \omega t \le \pi/6 \\ u_{\mathrm{dc}2} = -\frac{3R_{\mathrm{ac}}}{2}i_{\mathrm{dc}} - \frac{3L_{\mathrm{ac}}}{2}\frac{di_{\mathrm{dc}}}{dt} + \frac{3}{2}u_{a2}, \pi/6 \le \omega t \le \mu + \pi/6 \\ u_{\mathrm{dc}2} = -2R_{\mathrm{ac}}i_{\mathrm{dc}} - 2L_{\mathrm{ac}}\frac{di_{\mathrm{dc}}}{dt} + u_{a2} \\ \qquad -u_{c2}, \mu + \pi/6 \le \omega t \le \pi/3 \end{cases} \tag{26}$$

and when $\mu > \pi/6$, $u_{\mathrm{dc}2}$ can be expressed as follows:

$$\begin{cases} u_{\mathrm{dc}2} = -\frac{3R_{\mathrm{ac}}}{2}i_{\mathrm{dc}} - \frac{3L_{\mathrm{ac}}}{2}\frac{di_{\mathrm{dc}}}{dt} - \frac{3}{2}u_{b2}, 0 \le \omega t \le \mu - \pi/6 \\ u_{\mathrm{dc}2} = -2R_{\mathrm{ac}}i_{\mathrm{dc}} - 2L_{\mathrm{ac}}\frac{di_{\mathrm{dc}}}{dt} + u_{a2} \\ \qquad -u_{b2}, \mu - \pi/6 \le \omega t \le \pi/6 \\ u_{\mathrm{dc}2} = -\frac{3R_{\mathrm{ac}}}{2}i_{\mathrm{dc}} - \frac{3L_{\mathrm{ac}}}{2}\frac{di_{\mathrm{dc}}}{dt} + \frac{3}{2}u_{a2}, \pi/6 \le \omega t \le \pi/3 \end{cases} \tag{27}$$

REFERENCES

[1] S. Lauria, M. Schembari, F. Palone, and M. Maccioni, "Very long distance connection of gigawatt-size offshore wind farms: Extra high-voltage ac versus high-voltage dc cost comparison," *IET Renewable Power Gener.*, vol. 10, no. 5, pp. 713–720, May 2016.

[2] A. Nami, J. Liang, F. Dijkhuizen, and G. D. Demetriades, "Modular multilevel converters for HVDC applications: Review on converter cells and functionalities," *IEEE Trans. Power Electron.*, vol. 30, no. 1, pp. 18–36, Jan. 2015.

[3] R. Blasco-Gimenez, S. Añó-Villalba, J. Rodríguez-D'Derlée, F. Morant, and S. Bernal-Perez, "Distributed voltage and frequency control of offshore wind farms connected with a diode-based HVDC link," *IEEE Trans. Power Electron.*, vol. 25, no. 12, pp. 3095–3105, Dec. 2010.

[4] L. Yu, R. Li, and L. Xu, "Parallel operation of diode-rectifier based HVDC link and HVAC link for offshore wind power transmission," *J. Eng.*, vol. 2019, no. 18, pp. 4713–4717, Jul. 2019.

[5] J. C. Das, *Power System Harmonics and Passive Filter Designs*. Hoboken, NJ, USA: Wiley, 2015.

[6] Y. Chang and X. Cai, "Hybrid topology of a diode-rectifier-based HVDC system for offshore wind farms," *IEEE J. Emerg. Sel. Top. Power Electron.*, vol. 7, no. 3, pp. 2116–2128, Sep. 2019.

[7] T. H. Nguyen, D.-C. Lee, and C.-K. Kim, "A cost-effective converter system for HVDC links integrated with offshore wind farms," in *Proc. 39th Annu. Conf. IEEE Ind. Electron. Soc.*, 2013, pp. 7978–7983.

[8] T. H. Nguyen, D.-C. Lee, and C.-K. Kim, "A series-connected topology of a diode rectifier and a voltage-source converter for an HVDC transmission system," *IEEE Trans. Power Electron.*, vol. 29, no. 4, pp. 1579–1584, Apr. 2014.

[9] T. H. Nguyen, Q. A. Le, and D.-C. Lee, "A novel HVDC-link based on hybrid voltage-source converters," in *Proc. IEEE Energy Convers. Congr. Expo.*, Sep. 2015, pp. 3338–3343.

[10] J. Wang, J. Liang, F. Gao, X. Dong, C. Wang, and B. Zhao, "A closed-loop time-domain analysis method for modular multilevel converter," *IEEE Trans. Power Electron.*, vol. 32, no. 10, pp. 7494–7508, Oct. 2017.

[11] Z. Liu, J. Wang, L. Chen, Z. Wang, and Y. Jin, "A time-domain analysis model for modular-multilevel-based grid-forming converters in isolated power supply," *IEEE Trans. Power Electron.*, vol. 38, no. 5, pp. 6259–6271, May 2023.

[12] A. Jamshidifar and D. Jovcic, "Small-signal dynamic DQ model of modular multilevel converter for system studies," *IEEE Trans. Power Del.*, vol. 31, no. 1, pp. 191–199, Feb. 2016.

[13] Z. Li, Y. Pei, L. Wang, L. Zhao, L. Pei, and W. Cao, "A comprehensive closed-loop voltage ripple control scheme for modular multilevel converter-based power electronic transformers," *IEEE Trans. Power Electron.*, vol. 38, no. 12, pp. 15225–15241, Dec. 2023.

[14] Z. Xu, B. Li, S. Wang, S. Zhang, and D. Xu, "Generalized single-phase harmonic state space modeling of the modular multilevel converter with zero-sequence voltage compensation," *IEEE Trans. Ind. Electron.*, vol. 66, no. 8, pp. 6416–6426, Aug. 2019.

[15] J. Lyu, X. Zhang, X. Cai, and M. Molinas, "Harmonic state-space based small-signal impedance modeling of a modular multilevel converter with consideration of internal harmonic dynamics," *IEEE Trans. Power Electron.*, vol. 34, no. 3, pp. 2134–2148, Mar. 2019.

[16] J. C. Das, *Harmonic Generation Effects Propagation and Control*. Boca Raton, FL, USA: CRC Press, 2017.

[17] A. Moradi et al., "Detailed estimation of grid-side current and its oscillations caused by adjustable speed drive systems," *IEEE Trans. Ind. Electron.*, vol. 70, no. 9, pp. 8777–8787, Sep. 2023.

[18] L. Han, J. Wang, and D. Howe, "State-space average modelling of 6- and 12-pulse diode rectifiers," in *Proc. Eur. Conf. Power Electron. Appl.*, 2007, pp. 1–10.

[19] A. Griffo and J. Wang, "State-space average modelling of synchronous generator fed 18-pulse diode rectifier," in *Proc. 13th Eur. Conf. Power Electron. Appl.*, 2009, pp. 1–10.

[20] C. Liu, A. Bose, and P. Tian, "Modeling and analysis of HVDC converter by three-phase dynamic phasor," *IEEE Trans. Power Del.*, vol. 29, no. 1, pp. 3–12, Feb. 2014.

[21] A. Deriszadeh, O. Karabasoglu, M. P. Alasan, and F. Mehdipour, "A dynamic functional model of diode bridge rectifier for unbalanced input voltage conditions," *IET Power Electron.*, vol. 14, no. 3, pp. 584–589, Feb. 2021.

[22] G. Zhang, W. Xiang, M. Han, W. Zuo, M. Zhou, and J. Wen, "DC impedance modeling of push-pull DC auto-transformer for MMC and LCC HVDC interconnections," *IEEE Trans. Power Del.*, vol. 38, no. 4, pp. 2441–2453, Aug. 2023.

[23] R. Li and L. Xu, "A unidirectional hybrid HVDC transmission system based on diode rectifier and full-bridge MMC," *IEEE J. Emerg. Sel. Top. Power Electron.*, vol. 9, no. 6, pp. 6974–6984, Dec. 2021.

[24] U. C. Nwaneto and A. M. Knight, "Dynamic phasor-based modeling and simulation of a single-phase diode-bridge rectifier," *IEEE Trans. Power Electron.*, vol. 38, no. 4, pp. 4921–4936, Apr. 2023.

[25] L. Yu, R. Li, and L. Xu, "Distributed PLL-based control of offshore wind turbines connected with diode-rectifier-based HVDC systems," *IEEE Trans. Power Del.*, vol. 33, no. 3, pp. 1328–1336, Jun. 2018.

[26] C. T. Kelley, *Solving Nonlinear Equations With Newton's Method (Fundamentals of Algorithms)*. Philadelphia, PA, USA: SIAM, 2003.

[27] S. Li, X. Wang, Z. Yao, T. Li, and Z. Peng, "Circulating current suppressing strategy for MMC-HVDC based on nonideal proportional resonant controllers under unbalanced grid conditions," *IEEE Trans. Power Electron.*, vol. 30, no. 1, pp. 387–397, Jan. 2015.

[28] Q. Tu, Z. Xu, and L. Xu, "Reduced switching-frequency modulation and circulating current suppression for modular multilevel converters," *IEEE Trans. Power Del.*, vol. 26, no. 3, pp. 2009–2017, Jul. 2011.

[29] A. Dekka, B. Wu, R. L. Fuentes, M. Perez, and N. R. Zargari, "Evolution of topologies, modeling, control schemes, and applications of modular multilevel converters," *IEEE J. Emerg. Sel. Top. Power Electron.*, vol. 5, no. 4, pp. 1631–1656, Dec. 2017.

[30] Z. Li, Y. Pei, L. Chen, L. Wang, and J. Wang, "A novel inductance and capacitance selection method for modular multilevel converters based on modulation margin considerations," *IEEE J. Emerg. Sel. Top. Power Electron.*, vol. 12, no. 3, pp. 2431–2445, Jun. 2024.

Lu Chen (Student Member, IEEE) was born in Tangshan, China, in 1998. She received the B.S. degree in electrical engineering from Hebei University of Technology, Tianjin, China, in 2020. She is currently working toward the Ph.D. degree in electrical engineering with Xi'an Jiaotong University, Xi'an, China.

Her research interests include the topology, control, and design of wind power transmission systems, especially the modeling, design, and control of hybrid HVdc systems based on modular multilevel converters.

Jinyu Wang (Member, IEEE) received the B.S. degree in electrical engineering and the M.S. degree in power electronics from Jilin University, Changchun, China, in 2010 and 2013, respectively, and the Ph.D. degree in power systems from Shandong University, Jinan, China, in 2017.

From 2017 to 2020, he was a research fellow with Nanyang Technological University, Singapore. Since 2021, he has been a Full Professor in electrical engineering with Xi'an Jiaotong University, Xi'an, China. Since May 2022, he has been the Vice Chief Engineer with TBEA Xinjiang Sunoasis Company, Ltd., Xinjiang, China. His research interests include power electronics, multilevel converters, energy storage systems, renewable energy generation, and integration techniques, as well as stability analysis and control of modular-multilevel-converter based high-voltage dc.

Zhixiang Li (Graduate Student Member, IEEE) was born in Shandong, China, in 1996. He received the B.S. degree in electrical engineering in 2019 from Xi'an Jiaotong University, Xi'an, China, where he is currently working toward the Ph.D. degree in electrical engineering.

His research interests include the topology, control, and design of multilevel converters and isolated dc/dc converters, especially the control and design of power electronic transformers, the modular multilevel converters and the dual active bridge converters.

Chenyu Guo (Student Member, IEEE) was born in 2000. He received the B.S. degree in electrical engineering from Southwest Jiaotong University, Chengdu, China, in 2022. He is currently working toward the M.S. degree in electrical engineering with Xi'an Jiaotong University, Xi'an, China.

His research interests include modeling and control of modular multilevel converters.

Bobo Zhang (Student Member, IEEE) received the B.S. degree from the College of Electrical and Information Engineering, Hunan University, Changsha, China, in 2022. He is currently working toward the Ph.D. degree in electrical engineering with Xi'an Jiaotong University, Xi'an, China.

His research interests include multilevel converters and control of modular multilevel converter HVdc and dc grids.

Zhijie Li (Student Member, IEEE) was born in 2001. He received the B.S. degree in electrical engineering from North China Electric Power University, Baoding, China, in 2023. He is currently working toward the M.S. degree in electrical engineering with Xi'an Jiaotong University, Xi'an, China.

His research interests include the stability of grid-forming voltage source converters.